ACS APPLIED MATERIALS & INTERFACES

www.acsami.org

Research Article

Semiconductor Meta-Graphene and Valleytronics

Praveen Pai,* Aron W. Cummings,* Alexander Cerjan,* Wei Pan,* Fan Zhang,* and Catalin D. Spataru*

Cite This: *ACS Appl. Mater. Interfaces* 2026, 18, 6111−6121

Read Online

ACCESS | Metrics & More | Article Recommendations | Supporting Information

ABSTRACT: Nanopatterned semiconductor interfaces offer a versatile platform for creating quantum metamaterials and exploring novel electronic phenomena. In this study, we illustrate this concept using artificial graphene—a metamaterial featuring distinctive properties including Dirac and saddle points. We demonstrate that introducing additional nanopatterning can open a Dirac band gap, giving rise to what we term artificial hexagonal boron nitride (AhBN). The calculated valley Chern number of AhBN indicates the presence of topological valley Hall states confined to Dirac-gap domain walls. A key question is whether these one-dimensional edge states are topologically protected against disorder, given their vulnerability to Anderson localization. To this end, we perform band structure and electronic transport simulations under experimentally relevant disorder, including charge puddles and geometric imperfections. Our results reveal the resilience of the domain wall states against typical experimental disorder, particularly while the AhBN band gap remains open. The localization length along the domain wall can reach several microns—several times longer than the bulk electron mean free path—even though the number of bulk transport channels is greater. To enhance the effectiveness of the low-dissipation domain wall channel, we propose ribbon geometries with a large length-to-width ratio. These findings underscore both the potential and challenges of AhBN for low-energy, power-efficient microelectronic applications.

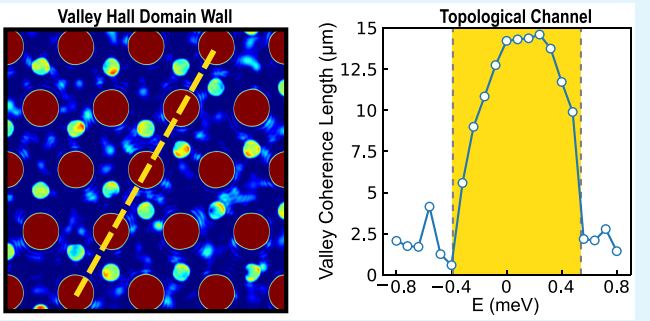

KEYWORDS: *valley Hall effect, Anderson localization, artificial graphene, 2D electron gas, antidot lattice, artificial quantum materials*

INTRODUCTION

Topological insulators (TIs)[1,2] are materials characterized by an insulating bulk but conducting surface, edge, or corner states. These dissipationless boundary modes arise from the contrast between the nontrivial topological invariant(s) of a TI's electronic structure and the trivial topology of states like the vacuum. This promise of efficient energy transfer mechanisms has generated significant interest in understanding how topological defects influence transport channels.[3] One such defect occurs when a two-dimensional (2D) material hosts a one-dimensional (1D) domain wall, characterized by a sharp discontinuity in a topological invariant across the interface. A key example of such an invariant is the valley Chern number,[4−8] a quantity associated with Berry curvature integrated over a single valley of an electronic band structure. The resulting valley Hall effect that arises from the difference of valley Chern numbers across a topological domain wall has been observed not only in bilayer graphene and transition-metal dichalcogenide electronic devices,[9−13] but also in acoustic and photonic crystals.[14−17] As the effect seems to be universal to both quantum and classical systems, it offers a promising avenue for practical energy or information transfer applications.

The performance of valley Hall systems based on traditional solid-state materials can, however, be challenged by the presence of disorder,[4] as has been recently demonstrated in the context of photonic topological interfaces.[18] One approach to address this issue involves implementing novel, tunable materials. In this context, we propose an innovative mechanism for realizing valleytronics on the surface of an industry-grade semiconductor using an advanced fabrication technology.

First, we consider artificial graphene (AG) as our primary quantum metamaterial. AG can be constructed by nano-engineering a 2D electron gas (2DEG) in a semiconductor heterostructure (such as AlSb/InAs/AlSb), and introducing a triangular antidot lattice via interferometric lithography.[19] The antidots repel electrons into regions of low potential, resulting in an effective honeycomb lattice where the pseudocarbon atoms are located. Because changing the nanopattern design is relatively straightforward, AG offers greater versatility than natural graphene. As a critical advantage, the AG lattice constant

Received: October 3, 2025
Revised: December 22, 2025
Accepted: December 23, 2025
Published: January 15, 2026

and the vertical depth of the patterned antidots may be strategically chosen. Then, we introduce secondary antidots in the pattern to open a bulk band gap in AG. As this mimics the structure of hexagonal boron nitride (hBN), we dub this metamaterial 'artificial hexagonal Boron Nitride' (AhBN). Opening a gap in this manner in a traditional graphene-like system reveals valley Chern numbers.[4−8] Therefore, we aim to understand the role of band topology and the effects of disorder on our AhBN system.

To investigate these effects, we first consider the introduction of disorder in the form of a fluctuating potential induced by hypothetical charge puddles.[20] As a semiconductor heterostructure contains nearby charge impurities or similar defects, analyzing the effect of this type of disorder is important for understanding how the valley Hall effect may survive under realistic conditions. Then, we consider a second type of disorder resulting from the geometrical variation in the nanopatterned antidots in the 2DEG that produce the AG/AhBN. Both types of disorder are relatively short-range for AG/AhBN, meaning that their relevant disorder length scales are shorter than the interpseudoatomic distance L; therefore, valley-Hall topological protection may be less effective, as it may not completely suppress intervalley scattering.[4] We analyze the impact of these types of disorder as a function of the disorder strength, on both the AhBN Dirac band gap and the Dirac-gap domain wall state.

Because the valley Chern number is not strictly quantized and the domain wall states are 1D in nature, they are susceptible to Anderson localization. We aim to understand the interplay between disorder-induced localization and the valley Hall effect, which provides some level of protection against localization. In particular, we seek to quantify the localization length of the domain wall state to accurately determine whether our system can demonstrate the valley Hall effect over length scales relevant to nano patterned devices. For realistic disorder strengths, we find that the localization length spans several microns, i.e., an order of magnitude larger than the AG periodicity L and significantly larger than the typical mean free path (<1 μm) of the underlying 2DEG. We are similarly encouraged by recent work displaying that the coherence of dissipationless 1D transport modes can be maintained up to 300 K,[21] thus opening a path toward room-temperature quantum information processing. Therefore, the proposed meta-graphene valley Hall states, combined with the wide tunability and ultrahigh quality of semiconducting superlattices, provide a promising platform for future applications in electronic devices with low-power dissipation.

RESULTS AND DISCUSSION

Artificial Graphene and Artificial hBN

The model for artificial graphene (AG) that we employ is the continuum model described by Park and Louie.[22] Figure 1(a) shows a typical Scanning electron microscope (SEM) image of AG with a lattice constant of L = 100 nm in an InAs quantum well. We use a triangular lattice of 'muffin tin' to represent the antidots as potential barriers that repel electrons. Along with the kinetic term describing an electron gas characterized by an effective mass m, we express the total Hamiltonian in a plane wave basis. Owing to its few intrinsic parameters, the model exhibits universal energy scaling in units of $\frac{h^2}{2mL^2}$. We maintain a consistent energy cutoff: $E_{cutoff} = 48\frac{h^2}{2mL^2} = 240$ meV throughout our continuum model calculations. A similar approach,

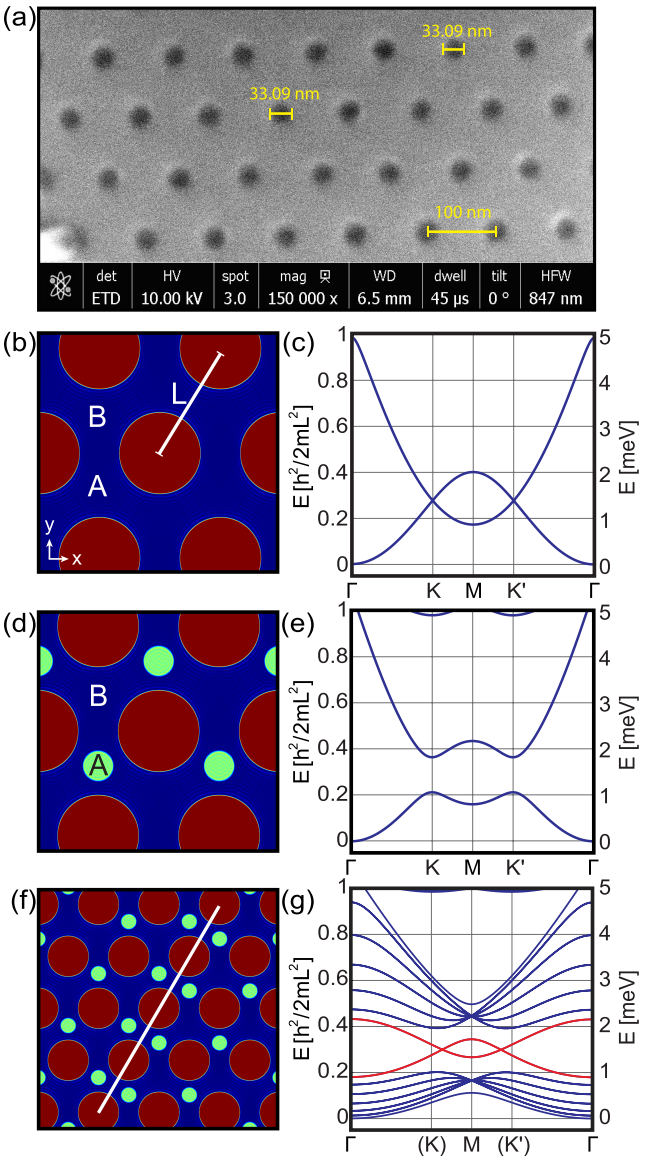

Figure 1. (a) SEM image of the experimentally produced AG with a lattice constant of L = 100 nm. (b) Potential profile of AG. The red holes (antidots) indicate potential barriers of strength V_1 that low-energy electrons cannot penetrate, resulting in the graphene-like band structure in (c). (d) Addition of holes of strength V_2 at the A sites of the lattice breaks inversion symmetry (and sublattice symmetry) and opens the band gap at the K/K' points, as indicated in the band structure in (e). (f) Potential profile of AhBN with a domain wall. The white line indicates the domain wall, which acts as a mirror line and contains an inversion center of the entire system. (g) The band structure projected along the domain wall direction that has a translational symmetry of AG. Each red band indicates a pair of domain wall states counter-propagating at the K/K' valleys; there are two parallel domain walls in our setup to ensure the periodic boundary condition.

utilizing a tight-binding basis, has recently been applied—and validated experimentally—to describe AG structures.[19,23] In our calculations, we set the potential strength of the primary triangular 'muffin-tin' lattice to $V_1 = 10\frac{h^2}{2mL^2}$. This nano patterning results in the formation of AG, with the pseudoatoms arranged in a conjugate honeycomb lattice, as indicated by the sites labeled A and B in Figure 1(b). In reciprocal space, this produces a graphene-like band structure with Dirac points at the

https://doi.org/10.1021/acsami.5c19865
ACS Appl. Mater. Interfaces 2026, 18, 6111−6121

K and K' points and saddle points at the three M points, as shown in Figure 1(c). The diameter of the antidots in our model is chosen to be $D_1 = \frac{L}{2}$, where L = 100 nm is the AG lattice constant. The antidots are expected to alter mostly the electronic behavior of 2DEG electrons with energies on the order of V_1, with the higher-energy electrons less affected. A secondary muffin-tin lattice with a potential strength V_2 is added at the A sites, breaking the inversion symmetry (and sublattice symmetry) between the A and B sites. Using $V_2 = 0.8\frac{h^2}{2mL^2}$ and diameter $D_2 = \frac{L}{4}$ opens a band gap $E_g = 0.15\frac{h^2}{2mL^2}$ at the K/K' Dirac points.[24] Although this energy gap only depends on the specific choice of V_2 and D_2, treating V_1 and V_2 as constants in units of $\frac{h^2}{2mL^2}$ while changing the lattice constant L does not modify $E_g = 0.15\frac{h^2}{2mL^2}$, since the kinetic term and both potential terms in the Hamiltonian share identical dimensional dependence on L. We term this gapped AG system 'artificial hexagonal Boron Nitride' (AhBN). Plots of the real-space potential profiles for AG and AhBN along with their low-energy bands are shown in Figure 1(b,d) and (c,e), respectively.

Breaking the inversion symmetry in graphene produces Berry curvature localized near the K/K' points. Because of time-reversal symmetry, the Berry curvatures at the two valleys are equal in magnitude but opposite in sign.[4,24] A similar phenomenon occurs in AG; in the insets of Figure 2 we

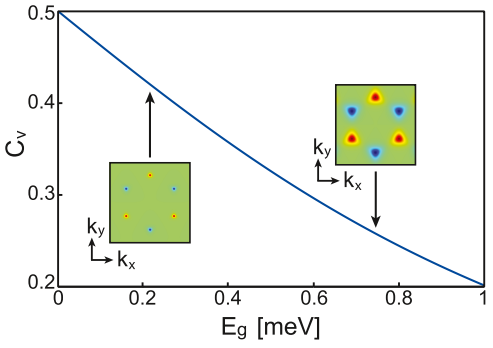

Figure 2. Plot of valley Chern number C_v versus energy band gap E_g. Insets: momentum-space distribution of the Berry curvature at indicated values of E_g. The regions exhibiting nonzero curvature correspond to the K/K' points. For $V_1 = 10\frac{h^2}{2mL^2}$, $V_2 = 0.8\frac{h^2}{2mL^2}$, $D_1 = \frac{L}{2}$, $D_2 = \frac{L}{4}$, and L = 100 nm, we obtain E_g = 0.76 meV and $C_v = \frac{1}{4}$.

illustrate how the Berry curvature seeps out of the K and K' points as the gap opens in AhBN. Additionally, we explicitly calculate the valley Chern numbers.[25] When the strength of the secondary potential approaches our chosen V_2, summing the Berry flux around each valley on a discretized mesh reveals that the valley Chern numbers reach approximately $C_v = \pm\frac{1}{4}$. It has recently been shown that photonic valley Hall states may, depending on the disorder type, exhibit significant back-scattering[18] even in the ideal limit of $C_v = \pm\frac{1}{2}$.[4,24] To explore the resilience of the valley-Hall effect in our semiconducting platform, we assess its robustness under experimentally relevant disorder.

Leveraging existing knowledge of topological transport and bulk-edge correspondence,[4,26] we juxtapose two regions of AhBN against each other, as indicated in Figure 1(f). Due to the nonzero difference between the valley Chern numbers on the two sides of the domain wall, this configuration is expected to produce topological edge states. Figure 1(g) shows the calculated band structure projected to the domain wall direction: there is a pair of in-gap states, counter-propagating at the two valleys and confined to its host domain wall. Note that, because of periodic boundary conditions, the supercell accommodates two parallel domain walls, resulting in two red bands of domain wall states in Figure 1(g).

Charge Puddle Disorder

To establish how robust these domain wall states are against disorder,[4,8,27] we first consider disorder whose length scale is much smaller than the lattice constant L, since L in our AG is on the mesoscopic scale. Adhering to the type of disorder observed in graphene experiments, we first analyze the effect of charge puddle disorder.[28] Note that while the charge puddles are smooth across the graphene lattice, they exhibit sublattice-scale variation in AG—a key distinction we emphasize.

We assume that the individual charge puddles take the form of Gaussians, with a standard deviation of σ = 5 nm for each charge puddle, and that there are 100 charge puddles per AG unit cell on average (this corresponds to a relatively dirty sample with 1.1 $\times 10^{12}$ puddles/cm^2). The total disorder strength U is defined as the standard deviation of a normal distribution from which the strength of the potential is sampled. Our calculations are performed using a 12 × 12 supercell for bulk AG and AhBN, and a 12 × 24 supercell for AhBN with two domain walls—corresponding to two 12 × 12 domains—ensuring periodic boundary conditions. In each configuration, we calculate the density of states (DOS) over a 12 × 12 Monkhorst–Pack k-point mesh[29] using a small Lorentzian broadening of 0.02 meV. We consider more than 150 random realizations of charge puddles, and two representative configurations are shown in Figure 3(a,c).

As shown in the DOS in Figure 3(b), the bulk band gap of AhBN remains open until the disorder strength U approaches the magnitude of the gap. Figure 3(d) shows the DOS of the AhBN system with two domains of opposite Dirac gaps. Evidently, a constant DOS persists within the gap until it is closed by disorder, indicating the presence of robust topological domain wall states. In Figure 3(e,f) we present the local DOS of typical domain wall states at the midgap energy (1.5 meV). We note that for both charge puddle disorders with strengths 0.12 and 0.3 meV, the domain wall states appear to be extended. Additionally, it is clear that the localization of these states increases with the disorder strength. We will provide a more quantitative assessment using transport simulations below.

Geometric Disorder

In addition to charge puddle disorder, we also account for random variations in the radii of individual antidots in our model, as this geometric aberration is relevant to the experimental construction of the AhBN system, as exemplified in Figure 4(a). We characterize the disorder strength by the maximum permitted deviation of the antidot radius from its unperturbed value, expressed as a percentage. The random radii are sampled from a uniform distribution within this range. Our DOS calculations for geometric disorder are performed using a 12 × 12 supercell for bulk AhBN, and a 12 × 24 supercell for AhBN with domain walls, utilizing approximately 200 random configurations.

https://doi.org/10.1021/acsami.5c19865
ACS Appl. Mater. Interfaces 2026, 18, 6111−6121

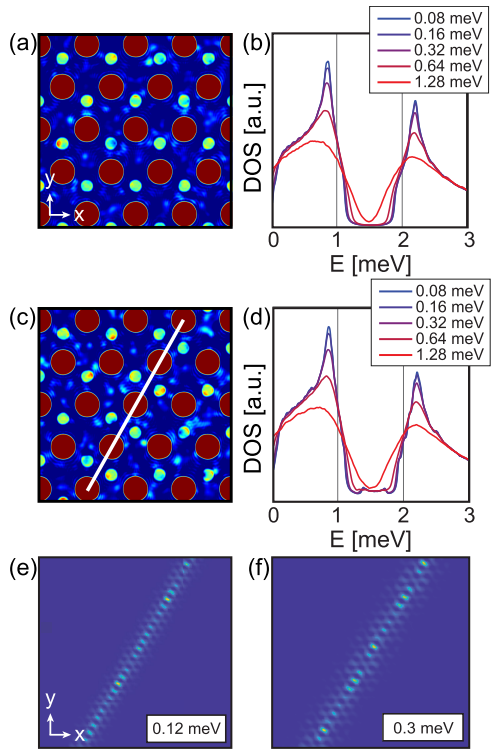

Figure 3. (a) Potential profile of AhBN with charge puddle disorder. (b) Calculated DOS for (a) at different disorder strengths. The bulk band gap closes at a critical disorder strength. (c) The same as (a) but with a domain wall. (d) Calculated DOS for (c) at different disorder strengths. The DOS within the bulk gap remains constant, indicating that the domain wall states survive on average until the disorder is sufficient to close the bulk gap. (e, f) Local DOS of the domain wall states at the midgap energy (1.5 meV) for two charge puddle configurations.

Figure 4(b,d) illustrate how both the bulk and domain wall real-space potentials may change under geometrical disorder for a particular random configuration. Figure 4(c) shows the calculated average DOS, indicating that the band gap does not close until there is a deviation of 20% from the perfect antidot lattice, which is significantly greater than the typically observed experimental deviation (≲5%). We further observe from Figure 4(e) that the finite DOS of the domain wall states signifies their presence within the gap, persisting up to the point at which the bulk gap closes. Figure 4(f,g) show the extended domain wall states at the midgap energy (1.5 meV) for geometric deviations of 2% and 8%. Similar to what is observed for charge puddle disorder, the domain wall states localize over several unit cells, and the localization increases with the deviation. Our DOS results allow us to refer to transport calculations for a more complete characterization of the localization of domain wall states.

Reflection Invariant and Topological Protection

In addition to AhBN exhibiting the valley Chern number, a reflection-symmetric domain wall is also associated with a topological invariant rendered by this symmetry. This invariant protects the existence of the interface-localized conduction channel against disorder that preserves the reflection symmetry. Furthermore, it also provides a measure of the protection—associated with the existence of the domain wall state—even in the presence of disorder that breaks this symmetry.

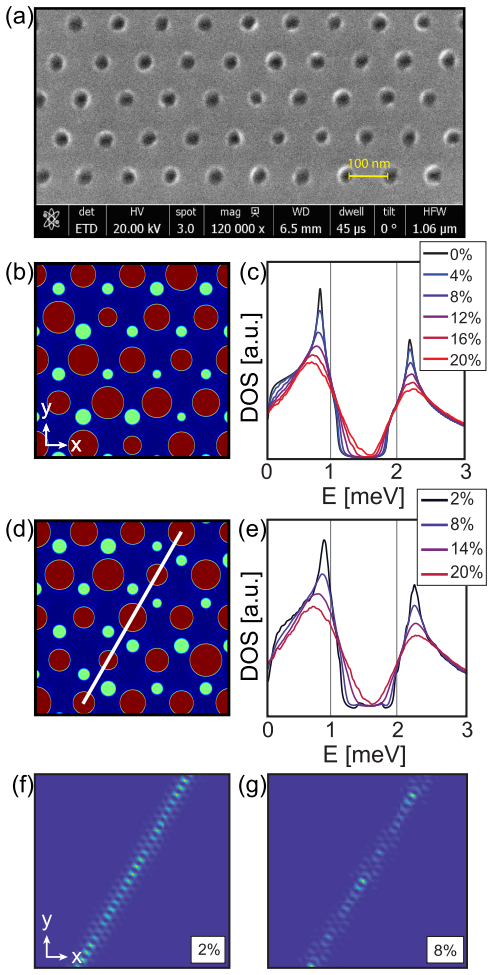

Figure 4. (a) SEM image of an AG sample exhibiting geometric disorder with a strength of approximately 9%. (b) Potential profile of AhBN with geometric disorder. (c) Calculated DOS for (b) at different disorder strengths, given in maximum percentage deviation of the antidot radius from the perfect case. (d) The same as (b) but with a domain wall. (e) Calculated DOS for (d) at different disorder strengths. (f, g) Local DOS of the domain wall states at the midgap energy (1.5 meV) for two geometric disorder configurations.

To classify the reflection-symmetric AhBN structure, we use the spectral localizer framework,[30−33] which provides both a suite of local topological markers and an associated measure of topological protection. In particular, a reflection-symmetric 2D structure can be classified using the symmetry-reduced spectral localizer[34]

$$\tilde{L}_E^{\mathcal{R}}(X, H) = (H - E\mathbf{1} + i\kappa X)\mathcal{R} \tag{1}$$

Here, X is the position operator in the direction perpendicular to the reflection symmetry $\mathcal{R}$, E is a choice of energy typically taken to be the Fermi energy, κ is a scaling parameter on the order of the bulk band gap divided by the length of the system in the x-direction, $\kappa \sim E_{\text{gap}}/L$, and $\mathbf{1}$ is the identity. As $X\mathcal{R} = -\mathcal{R}X$ and $\mathcal{H}\mathcal{R} = \mathcal{R}H$, $\tilde{L}_E^{\mathcal{R}}$ is Hermitian, and as such it possesses an energy-resolved integer invariant of matrix homotopy

$$\zeta_E^{\mathcal{R}}(X, H) = \frac{1}{2}\text{sig}[\tilde{L}_E^{\mathcal{R}}(X, H)] \in \mathbb{Z} \tag{2}$$

Here, sig[M] denotes the signature of a Hermitian matrix M, defined as its number of positive eigenvalues minus its number

https://doi.org/10.1021/acsami.5c19865
ACS Appl. Mater. Interfaces 2026, 18, 6111−6121

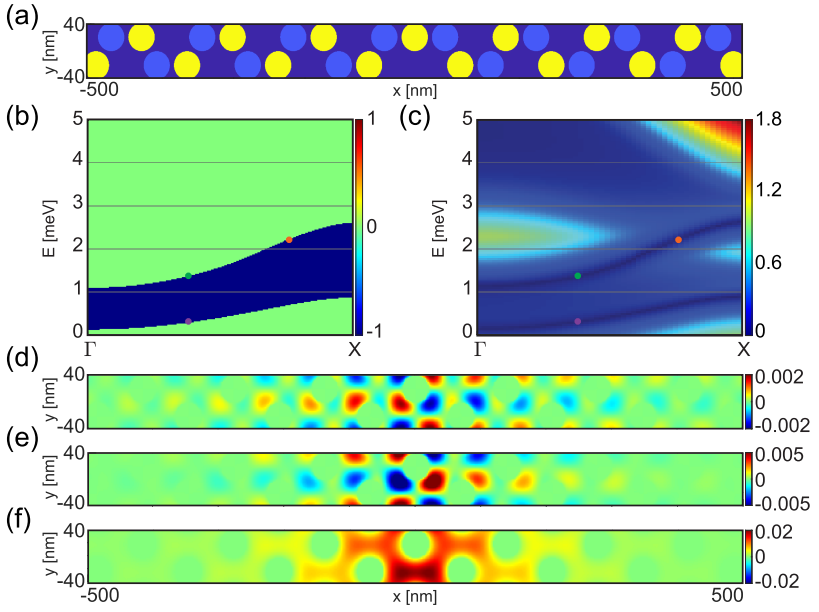

Figure 5. (a) Geometry of a reflection symmetric AhBN ribbon with a domain wall. (b)-(c) Energy-resolved marker $\zeta_E^{\mathcal{R}}$ (b) and local gap μ_E (c) as a function of energy E and wavevector k_y along the domain wall direction. (d)-(f) Wave functions $\mathrm{Re}[\psi_{(k_y,E)}(x)]$ of the topological domain wall-localized states at E = 1.37 meV (d), E = 2.21 meV (e), and E = 0.32 meV (f), which are marked by the green, orange, and purple dots in (b), (c), respectively.

of negative eigenvalues. As eigenvalues of Hermitian matrices must move continuously, sig[M] cannot change without one of its eigenvalues first becoming zero, i.e., without M becoming noninvertible. Thus, the eigenvalue of $\tilde{L}_E^{\mathcal{R}}$ closest to zero carries information about a system's topological protection against reflection-symmetry preserving perturbations. Specifically, the system's local gap can be defined as

$$\mu_E(X, H) = \min(|\mathrm{spec}[\tilde{L}_E^{\mathcal{R}}(X, H)]|) \tag{3}$$

which by Weyl's inequality[35,36] requires that a change in the system's topology is only possible if a symmetry-preserving perturbation δH is strong enough to close the local gap, $\|\delta H\| > \mu_{(x,E)}$. Here, spec[M] denotes the spectrum of M. Finally, bulk-boundary correspondence manifests in the spectral localizer framework because closings of the local gap, where $\mu_E \approx 0$, guarantee the existence of nearby states.[37] Altogether, eq 2 distinguishes reflection-symmetric systems based on whether their associated spectral localizers can be path-continued to one another while remaining invertible and preserving $\mathcal{R}$.

To demonstrate the topology associated with the domain wall in AhBN, we consider a reflection-symmetric ribbon of AhBN that we simulate using the approach in,[23] assuming L = 80 nm. We consider open boundary conditions along the x-direction and periodic boundary conditions along the y-direction as shown in Figure 5(a). Thus, we can use $\zeta_E^{\mathcal{R}}(X, H(k_y))$ and $\mu_E(X, H(k_y))$ to classify the system's topology and associated protection, choosing $\mathcal{R}$ to be the mirror symmetry along the domain wall. In doing so, we numerically observe that the change in the topological index and gap closing correspond to the domain wall-localized state, as seen in Figure 5(b−f).

Of course, experimentally relevant fabrication disorder is not reflection symmetric. Nevertheless, the in-gap domain wall-localized states still exhibit some lingering protection stemming from Weyl's inequality. To demonstrate this remnant of protection, we consider the full spectral localizer for a 2D system

$$L_{(x,y,E)}(X, Y, H) = \begin{bmatrix} H - E\mathbf{1} & \kappa(X - x\mathbf{1}) - i\kappa(Y - y\mathbf{1}) \\ \kappa(X - x\mathbf{1}) + i\kappa(Y - y\mathbf{1}) & -(H - E\mathbf{1}) \end{bmatrix} \tag{4}$$

and corresponding local gap

$$\mu_{(x,y,E)}(X, Y, H) = \min(|\mathrm{spec}[L_{(x,y,E)}(X, Y, H)]|) \tag{5}$$

Here, X and Y are the position operators of the 2D system, and (x, y, E) is a choice of location in position-energy space where the spectral localizer and local gap are being evaluated. The key point is that locations where $\mu_{(x,y,E)} \approx 0$ still guarantee the existence of nearby states, regardless of whether the system exhibits any nontrivial topological index. Moreover, the rate at which $\mu_{(x,y,E)}$ can change in response to perturbations to the system is still bound by Weyl's inequality[33]

$$|\mu_{(x,y,E)}(X, Y, H + \delta H) - \mu_{(x,y,E)}(X, Y, H)| \leq \|\delta H\| \tag{6}$$

where now δH is an arbitrary perturbation to the system's Hamiltonian that need not preserve any symmetries.

The robustness of the domain wall-localized states in AhBN can be confirmed using a large-but-finite 2D AhBN lattice, shown in Figure 6(a). Here, the local gap of the clean system approaches zero along the domain wall at energies where the topological index changes, Figure 6(d).

We next consider a disorder potential induced by charge puddles. As above, each individual charge puddle is modeled as a Gaussian with a standard deviation of σ = 5 nm, and the concentration of charge puddles is $10^{12}/\mathrm{cm}^2$. The total disorder strength U is defined as the standard deviation of a normal distribution from which the potential strength is sampled. Upon addition of disorder, examples of which are shown in Figure 6(b,c), the near closing of the local gap is seen to persist, Figure 6(e−h), demonstrating the robustness of the domain wall-

https://doi.org/10.1021/acsami.5c19865
ACS Appl. Mater. Interfaces 2026, 18, 6111−6121

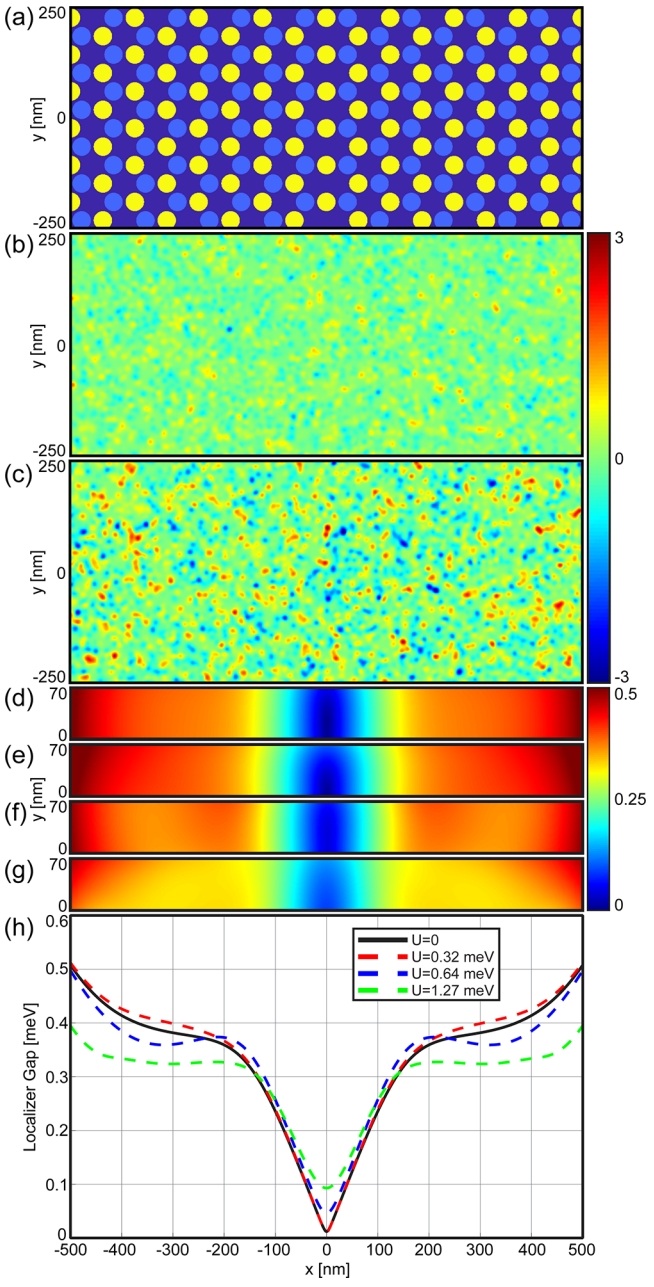

Figure 6. (a) Geometry of a finite AhBN flake with a reflection-symmetric domain wall in the absence of disorder. (b), (c) Distribution of the added charge puddle disorder with standard deviation $\sigma = 5$ nm, 10^{12} charge puddles/cm^2, and disorder strength $U = 0.32$ meV (b) and $U = 0.64$ meV (c). (d)−(g) Local gap $\mu_{(x,y,E)}$ at fixed energy for $U = 0$ (d), $U = 0.32$ meV (e), $U = 0.64$ meV (f), and $U = 1.27$ meV (g). (h) Line cuts of $\mu_{(x,y,E)}$ for fixed $y = 0$ and $E = 1.5$ meV, for values of U from (d)−(g). The contribution to $\mu_{(0,y,E)}$ from disorder is negligible until U approaches E_{gap}.

localized states against arbitrary disorder, though without providing any guarantees on the conductivity that these states may provide. Note, as the symmetry protecting the topology is broken by the disorder, $\zeta_E^{\mathcal{R}}(X, H + \delta H)$ is no longer well-defined as when $[\delta H, \mathcal{R}] \neq 0$, $\tilde{L}_E^{\mathcal{R}}(X, H + \delta H)$ is not Hermitian. A quantitative assessment of their conductive properties requires transport simulations.

Transport Simulations

We now examine disorder on the scale of the AG lattice constant L, and its impact on transport through the domain wall state. We treat the disorder by first reducing the AhBN system to a single-orbital tight-binding representation on a honeycomb lattice, with the Hamiltonian

$$\hat{H} = \sum_i \varepsilon_i^{A/B} \hat{c}_i^\dagger \hat{c}_i + \sum_{\langle ij \rangle} t_{ij} \hat{c}_i^\dagger \hat{c}_j, + \sum_i \varepsilon_i^{dis} \hat{c}_i^\dagger \hat{c}_i \tag{7}$$

where $\hat{c}_i^\dagger$ ($\hat{c}_i$) is the creation (annihilation) operator of an electron at honeycomb lattice site i. The band gap of AhBN is captured by the on-site potential $\varepsilon_i^{A/B} = \pm \Delta/2$ at lattice sites A and B respectively, while t_{ij} is the hopping between the nearest neighbor sites i and j. To capture lattice-scale disorder, we include the third term and employ an Anderson model for ε_i^{dis},[38,39] where the potential of each lattice site is shifted by a random value. Here the random disorder potential is chosen according to a normal distribution centered around the midgap (the zero-energy reference) with standard deviation U. To model the AhBN lattice in Figure 1, we set $\Delta = 0.78$ meV, $t_{ij} = 0.85$ meV, and $L = 100$ nm. These values of t_{ij} and Δ were chosen to match the bandwidth and bulk gap of our continuum model for AhBN respectively. As the charge puddle disorder investigated above features variation smaller than the lattice constant ($\sigma/L < 1$), our tight-binding representation of AhBN can only capture the geometric disorder of the antidots. Because disorder in the hopping parameters t_{ij} cannot capture the change in the bulk AhBN band gap (see Supporting Information), we implement on-site disorder in our transport simulations. In the Supporting Information, we show that adding hopping disorder on top of on-site disorder does not affect any of the trends discussed here.

To calculate transport through the domain wall state, we use the setup depicted in Figure 7(a), built using the *pybinding* package.[40] We consider a finite channel of AhBN, with the color indicating the staggered on-site potential at each lattice site. For the top half of the channel we set $\varepsilon_i^{A/B} = \pm \Delta/2$ and the opposite sign for the bottom half, thereby forming a domain wall at $y = 0$. For the purpose of visualization, only a relatively narrow channel is shown in Figure 7(a). In our transport simulations we consider channels with widths of $W = 200$ $L = 20$ μm and $W = 10$ $L = 1$ μm, while varying the channel length L_{ch} up to $L_{ch} = 10$ μm.

We calculate the transmission from the left to the right of the channel, from lead 0 to lead 1, using the Landauer-Büttiker formalism implemented in the *kwant* simulation package.[41] For a given disorder strength U, we calculate the energy- and channel length-dependent conductance $G(E, L_{ch}) = 2e^2/h \cdot T(E, L_{ch})$, where T is the transmission, e is the electron charge, and h is Planck's constant.[42] For each channel length we consider 200 random disorder configurations, from which we calculate the typical conductance $G_{typ} = \exp(\langle \ln(G) \rangle)$, where $\langle \cdots \rangle$ indicates the disorder average.[43,44] We then extract the energy- and channel length-dependent resistance as $R(E, L_{ch}) = 1/G_{typ}(E, L_{ch})$. In all the cases we consider relatively weak disorder, $U = \Delta/6 = 0.13$ meV, which is expected to preserve the band gap and the domain wall state.

Bulk Limit. First we consider a very wide system, with a channel width $W = 200L = 20$ μm, to mimic the bulk limit of AhBN. Figure 7(b) shows the band structure of this setup in the absence of disorder. Similar to Figure 1(f), the bulk bands have a gap of $\Delta = 0.78$ meV, and the domain wall state (shown in red) traverses the gap. The flat bands at $E \approx -0.39$ meV correspond

https://doi.org/10.1021/acsami.5c19865
ACS Appl. Mater. Interfaces 2026, 18, 6111−6121

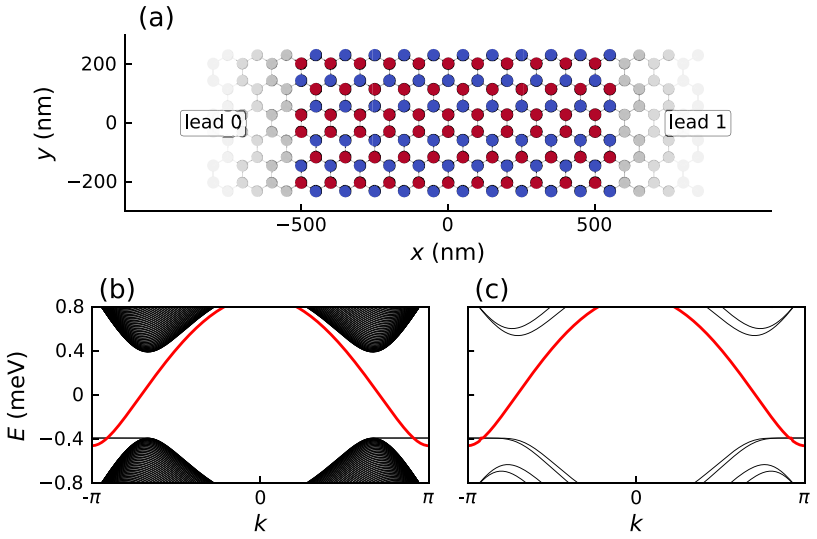

Figure 7. (a) Setup for the transport simulations, which calculate transmission from lead 0 to lead 1. Red/blue lattice sites correspond to an on-site energy of $\pm \Delta/2$. (b) Band structure of the system in panel (a) for a channel width of 20 μm. Black bands indicate the bulk bands of AhBN, while the red band indicates the domain wall state localized around $y = 0$. (c) The same as (b) but for a channel width of 1 μm.

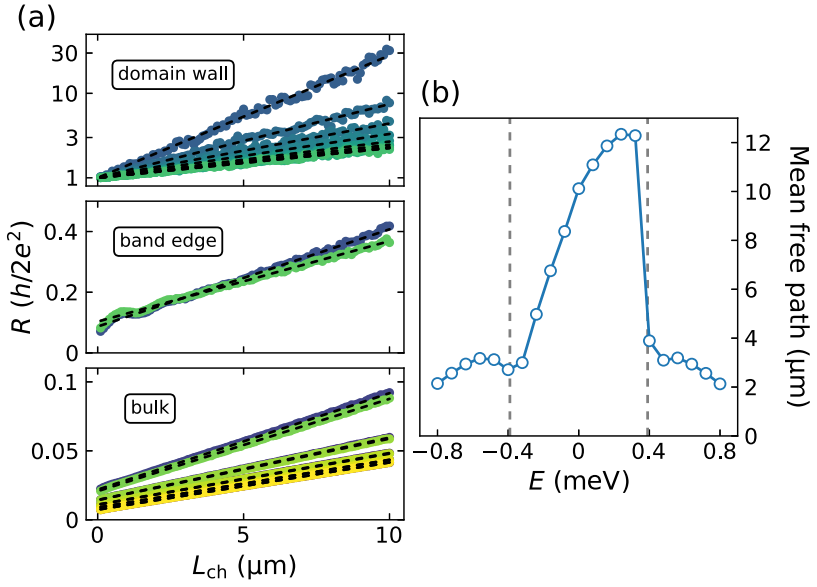

Figure 8. (a) Resistance of AhBN vs channel length for a wide channel ($W = 20$ μm) with a disorder strength of $U = \Delta/6 = 0.13$ meV. The top panel is for states within the bulk band gap ($|E| < 0.39$ meV), corresponding to the domain wall state. The middle panel is for states near the band edges ($|E| = 0.39$ meV), and the bottom panel is for bulk states ($|E| > 0.39$ meV). Colored symbols are numerical data, and black dashed lines are fits to extract the mean free path. (b) Mean free paths extracted from (a), indicating enhanced transport in the domain wall state compared to the bulk states. The vertical dashed lines mark the band edges.

to the zigzag edge states on the top and bottom edges of the channel. In Figure 8(a) we show the length-dependent resistance over a range of energies ($|E| < 0.8$ meV). As indicated by the labels, the highest resistance corresponds to energies associated with the midgap domain wall state ($|E| < 0.39$ meV), the next group of curves corresponds to energies near the band edge ($|E| = 0.39$ meV), and the lowest-resistance curves correspond to the bulk states in the conduction and valence bands ($|E| > 0.39$ meV).

At short channel lengths, the resistance is determined by the number of modes available for transport. This is why the domain wall state has the highest resistance—within the band gap there is only one mode. To better compare the transport properties across all energies, we use the scaling of R vs L_{ch} to extract the mean free path. In the bulk and at the band edges, the resistance increases linearly with channel length, as seen in the middle and bottom panels of Figure 8(a). In this ohmic regime of transport, the mean free path can be extracted by fitting the simulation data to[42]

$$R(E, L_{ch}) = R_c(E)\left(1 + \frac{L_{ch}}{l_{mfp}(E)}\right) \tag{8}$$

where R_c is the contact resistance and l_{mfp} is the mean free path. The black dashed curves in Figure 8(a) indicate the fits to the numerical data.

Meanwhile, within the band gap the resistance of the domain wall state increases exponentially with channel length, as

https://doi.org/10.1021/acsami.5c19865
ACS Appl. Mater. Interfaces 2026, 18, 6111−6121

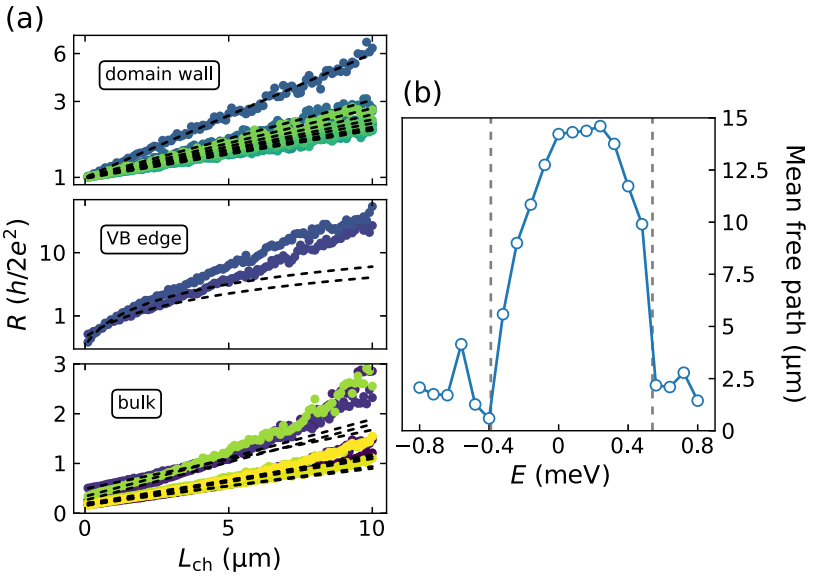

Figure 9. (a) Resistance of AhBN vs channel length for a narrow channel ($W = 1\ \mu$m) with a disorder strength of $U = \Delta/6 = 0.13$ meV. The top panel is for states within the bulk band gap ($-0.39 < E < 0.54$ meV), corresponding to the domain wall state. The middle panel is for states near the valence band edge ($E = -0.4$ and -0.48 meV), and the bottom panel is for bulk states ($E < -0.48$ and $E > 0.54$ meV). Colored symbols are numerical data, and black dashed lines are fits to extract the mean free path. (b) Mean free path extracted from (a), indicating enhanced transport in the domain wall state compared to the bulk states. The vertical dashed lines mark the band edges.

indicated in the top panel of Figure 8(a). This is consistent with transport in a 1D channel, where the exponential scaling may be directly connected to the mean free path.[44,45] For the case of one propagating mode, the mean free path can be extracted from[44]

$$R(E, L_{ch}) = \frac{h}{2e^2}\exp(L_{ch}/l_{mfp}(E)) \tag{9}$$

We plot the energy-dependent mean free path in Figure 8(b). Within the bulk, the mean free path falls within 2−3 μm. Meanwhile, it reaches more than 12 μm within the band gap, indicating the relative robustness of the domain wall state against weak disorder. However, despite the longer mean free path at the interface, the overall resistance remains much lower in the bulk AhBN region due to the larger number of modes available for transport.

AhBN Ribbon. In the previous subsection we have revealed that while the mean free path of the topological interface state is much higher than that of the AhBN bulk states, the overall resistance is also much higher for the interface state because of the single mode nature. This then raises the question: is there a situation where the midgap domain wall state shows comparable or better transport properties compared to the bulk of AhBN? In principle, this may be achieved in a much narrower system, as lateral confinement should reduce the number of bulk conduction modes and could also degrade the bulk transport properties. We examine this here by considering the same setup as before but with a channel width of 10 unit cells, $W = 10$ $L = 1$ μm.

Figure 7(c) shows the band structure of this narrower system, which is similar to that of the wider system shown in Figure 7(b), but with a few key changes. First, the number of subbands in the bulk is significantly reduced, which will lead to a significant increase in the bulk resistance. Second, owing to the lateral confinement, the size of the band gap has increased a bit, to the range $-0.39 < E < 0.54$ meV. Figure 9 shows the length-dependent resistance and the mean free path of this narrower system. The domain wall states exhibit localized transport similar to the case of the wider system. By contrast, the states in the bulk and at the band edge, which are ohmic in the case of the wider system, now exhibit a metal-to-insulator transition at a channel length of a few microns. In Figure 9(b) we plot the mean free path, extracted using the same procedure as before. For the bulk and band-edge states we fit eq 8 to the resistance for $L_{ch} < 1$ μm, for which transport is still in the ohmic regime[1]. Evidently, the mean free paths of the domain wall state and the bulk states remain similar to the wider channel case, with the former slightly increased and the latter slightly reduced.

Owing to the metal-to-insulator transition, as well as the reduced number of modes available for transport, the resistance of the bulk AhBN states is much higher in this narrower system than in the wider one, with the resistance being comparable to that in the bulk gap. Therefore, a narrower channel appears to be a system where a topological interface state can provide a transport advantage over the bulk AhBN.

CONCLUSIONS

We have demonstrated that nanopatterned meta-graphene can exhibit a designable band gap at the Dirac point, giving rise to an artificial analog of hexagonal boron nitride with nontrivial valley-projected band topology. Through an investigation of the DOS of the domain wall edge state and the behavior of both the spectral localizer and the local gap in the presence of two disorder mechanisms, we have sought to test the robustness of our domain wall state through transport simulations. Our numerical analysis shows that the domain wall state in AhBN remains robust even in the presence of experimentally relevant disorder, with localization lengths reaching beyond ten microns, extending substantially longer than the bulk mean free path. We further emphasize that the mean free path estimated in our transport calculations was obtained under deliberately dirty conditions. As a result, the true mean free path in experimentally optimized, high-mobility samples is expected to exceed the value displayed in Figure 8(b). These results suggest that while topological transport mediated by the domain wall states is

https://doi.org/10.1021/acsami.5c19865
ACS Appl. Mater. Interfaces 2026, 18, 6111−6121

resilient, practical implementation is limited by residual bulk conduction. As such, we propose that high aspect ratio ribbon geometries can enhance the domain wall-dominated transport, offering a viable route toward integrating such systems in quantum information and microelectronic applications. To achieve these applications, electron-beam lithography can be used to fabricate the domain wall structure and position electrodes near its two ends. The two-terminal conductance can then be measured to detect possible quantization and to extract the valley-coherence length. Future technologies may utilize dissipationless 1D transport in the domain wall between different lateral patterns for quantum information processing. Moreover, by creating lateral lithography-defined patterns from the mature technology of semiconductor heterostructures, new quantum electronic devices will be set on a path toward high-order integration, leveraging decades of semiconductor industry development.

While our work has focused on transport with relatively high geometric and charge puddle disorder compared to experimental disorder broadening (see Experimental Section), our computational study establishes a lower bound on the mean free path of these edge modes. Consequently, our platform provides a means of realizing electronic highways[8] with extended propagation lengths. These highways arise from the edge modes' ability to follow well-defined paths despite kinks and imperfections in the channel geometry. We therefore predict that the AhBN platform enables guided, low-dissipation electronic pathways, offering a practical building block for engineered valleytronic devices at scales smaller than the mean free path of the underlying 2DEG, which in high-mobility GaAs quantum wells can reach a few hundred microns.[46] See Figure 10 for a schematic illustration of an electronic highway.

Taken together, these considerations indicate that our metagraphene platform provides a versatile foundation for realizing valleytronic functionalities within a unified, highly tunable architecture compatible with standard semiconductor-industry fabrication processes.

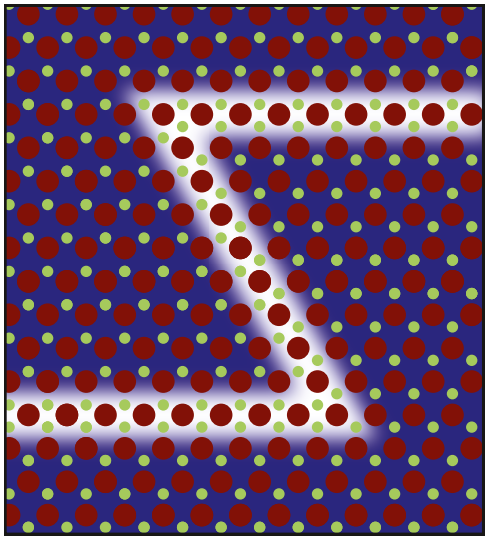

Figure 10. Schematic of electronic highways in our AhBN 2DEG. Here, zigzag edges at corners correspond to the domain wall edge modes discussed in this paper, illustrating how these channels can be routed and exploited in device geometries. The red circles indicate antidots controlled by V_1, and the green dots indicate holes controlled by V_2.

EXPERIMENTAL SECTION

AG was fabricated by nanopatterning a high-mobility 2DEG hosted in an AlSb/InAs/AlSb semiconductor quantum well heterostructure. The AG lattice was defined using interferometric lithography, which enables uniform large-area patterning of periodic nanostructures. This technique was employed to produce a triangular lattice of surface antidots that modulate the underlying 2DEG potential landscape and generate a graphene-like electronic band structure. Our theoretical modeling shows that the energy gap in our proposed lateral patterns is larger than both the disorder-induced broadening (approximately 0.2 meV) in our high-quality semiconductor structures and the thermal broadening (approximately 0.03 meV at 0.3 K).

ASSOCIATED CONTENT

Supporting Information

The Supporting Information is available free of charge at https://pubs.acs.org/doi/10.1021/acsami.5c19865.

Transport results including hopping disorder for the tight-binding Anderson model and the band structure associated with Figure 5(PDF)

AUTHOR INFORMATION

Corresponding Authors

Praveen Pai − *Department of Physics, University of Texas at Dallas, Richardson, Texas 75080, United States;* orcid.org/0009-0004-5143-1369; Email: praveen.pai@utdallas.edu

Aron W. Cummings − *Catalan Institute of Nanoscience and Nanotechnology (ICN2), CSIC and BIST, Bellaterra, Barcelona 08193, Spain;* orcid.org/0000-0003-2307-497X; Email: aron.cummings@icn2.cat

Alexander Cerjan − *Center for Integrated Nanotechnologies, Sandia National Laboratories, Albuquerque, New Mexico 87185, United States;* orcid.org/0000-0002-4362-7300; Email: awcerja@sandia.gov

Wei Pan − *Sandia National Laboratories, Livermore, California 94551, United States;* orcid.org/0000-0002-5629-5296; Email: wpan@sandia.gov

Fan Zhang − *Department of Physics, University of Texas at Dallas, Richardson, Texas 75080, United States;* Email: zhang@utdallas.edu

Catalin D. Spataru − *Sandia National Laboratories, Livermore, California 94551, United States;* Email: cdspata@sandia.gov

Complete contact information is available at: https://pubs.acs.org/10.1021/acsami.5c19865

Notes

The authors declare no competing financial interest.

ACKNOWLEDGMENTS

The authors acknowledge support from the Laboratory Directed Research and Development program at Sandia National Laboratories. This work was performed, in part, at the Center for Integrated Nanotechnologies, an Office of Science User Facility operated for the U.S. Department of Energy (DOE) Office of Science. Sandia National Laboratories is a multimission laboratory managed and operated by National Technology and Engineering Solutions of Sandia, LLC, a wholly owned subsidiary of Honeywell International, Inc., for the U.S. DOE's National Nuclear Security Administration under Contract No. DE-NA-0003525. ICN2 is funded by the CERCA Programme Generalitat de Catalunya and supported

by the Severo Ochoa Centres of Excellence programme, Grant CEX2021-001214-S, funded by MCIN/AEI/10.13039.501100011033. P.P. and F.Z. (UT Dallas) were supported by the NSF under grants DMR-2414726, DMR-1945351, and DMR-2324033 and by the Welch Foundation under grant AT-2264-20250403. P.P. and F.Z. acknowledge the Texas Advanced Computing Center (TACC) for providing supercomputing resources.

ADDITIONAL NOTE

[1]We find the same mean free path by fitting to eq 9, in the localized regime for $L_{ch} > 5\ \mu m$ and scaling by the number of modes N, $l_{mfp} \rightarrow l_{mfp} \cdot 2/(N+1)$[44]

REFERENCES

(1) Hasan, M. Z.; Kane, C. L. *Colloquium*: Topological Insulators. *Rev. Mod. Phys.* **2010**, *82*, 3045−3067.
(2) Moore, J. E. The Birth of Topological Insulators. *Nature* **2010**, *464*, 194−198.
(3) Teo, J. C. Y.; Kane, C. L. Topological Defects and Gapless Modes in Insulators and Superconductors. *Phys. Rev. B* **2010**, *82*, No. 115120.
(4) Zhang, F.; MacDonald, A. H.; Mele, E. J. Valley Chern numbers and boundary modes in gapped bilayer graphene. *Proc. Natl. Acad. Sci. U.S.A.* **2013**, *110*, 10546−10551.
(5) Martin, I.; Blanter, Y.; Morpurgo, A. F. Topological Confinement in Bilayer Graphene. *Phys. Rev. Lett.* **2008**, *100*, No. 036804.
(6) Zhang, F.; Jung, J.; Fiete, G. A.; Niu, Q.; MacDonald, A. H. Spontaneous Quantum Hall States in Chirally Stacked Few-Layer Graphene Systems. *Phys. Rev. Lett.* **2011**, *106*, No. 156801.
(7) Yao, W.; Yang, S. A.; Niu, Q. Edge States in Graphene: From Gapped Flat-Band to Gapless Chiral Modes. *Phys. Rev. Lett.* **2009**, *102*, No. 096801.
(8) Qiao, Z.; Jung, J.; Niu, Q.; MacDonald, A. H. Electronic Highways in Bilayer Graphene. *Nano Lett.* **2011**, *11*, 3453−3459.
(9) Alden, J. S.; Tsen, A. W.; Huang, P. Y.; Hovden, R.; Brown, L.; Park, J.; Muller, D. A.; McEuen, P. L. Strain Solitons and Topological Defects in Bilayer Graphene. *Proc. Natl. Acad. Sci. U.S.A.* **2013**, *110*, 11256−11260.
(10) Ju, L.; Shi, Z.; Nair, N.; Lv, Y.; Jin, C.; Velasco, J.; Ojeda-Aristizabal, C.; Bechtel, H. A.; Martin, M. C.; Zettl, A.; Analytis, J.; Wang, F. Topological Valley Transport at Bilayer Graphene Domain Walls. *Nature* **2015**, *520*, 650−655.
(11) Huang, K.; Fu, H.; Watanabe, K.; Taniguchi, T.; Zhu, J. High-Temperature Quantum Valley Hall Effect with Quantized Resistance and a Topological Switch. *Science* **2024**, *385*, 657−661.
(12) Zhu, T.; Ruan, W.; Wang, Y. Q.; et al. Imaging Gate-Tunable Tomonaga-Luttinger Liquids in 1H-MoSe2Mirror Twin Boundaries. *Nat. Mater.* **2022**, *21*, 748−753.
(13) Deng, B.; Ahn, H.; Wang, J.; Moon, G.; Han, C.; Dongre, N.; Lei, C.; Scuri, G.; Sung, J.; Brutschea, E.; Watanabe, K.; Taniguchi, T.; Zhang, F.; Jo, M.-H.; Park, H. Epitaxially Defined Luttinger Liquids on MoS 2 Bicrystals. *Phys. Rev. Lett.* **2025**, *134*, No. 046301.
(14) Lu, J.; Qiu, C.; Ye, L.; Fan, X.; Ke, M.; Zhang, F.; Liu, Z. Observation of topological valley transport of sound in sonic crystals. *Nat. Phys.* **2017**, *13*, 369−374.
(15) Gao, F.; Xue, H.; Yang, Z.; Lai, K.; Yu, Y.; Lin, X.; Chong, Y.; Shvets, G.; Zhang, B. Topologically protected refraction of robust kink states in valley photonic crystals. *Nat. Phys.* **2018**, *14*, 140−144.
(16) Yang, Y.; Yamagami, Y.; Yu, X.; Pitchappa, P.; Webber, J.; Zhang, B.; Fujita, M.; Nagatsuma, T.; Singh, R. Terahertz topological photonics for on-chip communication. *Nat. Photonics* **2020**, *14*, 446−451.
(17) Zhang, F. Brought to Light. *Nat. Phys.* **2018**, *14*, 111−113.
(18) Rosiek, C. A.; Arregui, G.; Vladimirova, A.; Albrechtsen, M.; Vosoughi Lahijani, B.; Christiansen, R. E.; Stobbe, S. Observation of strong backscattering in valley-Hall photonic topological interface modes. *Nat. Photonics* **2023**, *17*, 386−392.
(19) Pan, W.; Burckel, D. B.; Spataru, C. D.; et al. Lithography-Defined Semiconductor Moirés with Anomalous In-Gap Quantum Hall States. *Nano Lett.* **2025**, *25*, 10536−10543.
(20) Das Sarma, S.; Adam, S.; Hwang, E. H.; Rossi, E. Electronic Transport in Two-Dimensional Graphene. *Rev. Mod. Phys.* **2011**, *83*, 407−470.
(21) Wu, Z.; Zhou, B. T.; Cai, X.; et al. Intrinsic valley Hall transport in atomically thin MoS2. *Nat. Commun.* **2019**, *10*, No. 611.
(22) Park, C.-H.; Louie, S. G. Making Massless Dirac Fermions from a Patterned Two-Dimensional Electron Gas. *Nano Lett.* **2009**, *9*, 1793−1797.
(23) Spataru, C. D.; Pan, W.; Cerjan, A. Topological Phenomena in Artificial Quantum Materials Revealed by Local Chern Markers. *Phys. Rev. Lett.* **2025**, *134*, No. 126601.
(24) Xiao, D.; Chang, M.-C.; Niu, Q. Berry phase effects on electronic properties. *Rev. Mod. Phys.* **2010**, *82*, 1959−2007.
(25) Fukui, T.; Hatsugai, Y.; Suzuki, H. Chern Numbers in Discretized Brillouin Zone: Efficient Method of Computing (Spin) Hall Conductances. *J. Phys. Soc. Jpn.* **2005**, *74*, 1674−1677.
(26) Hatsugai, Y. Chern number and edge states in the integer quantum Hall effect. *Phys. Rev. Lett.* **1993**, *71*, 3697−3700.
(27) Li, J.; Martin, I.; Büttiker, M.; Morpurgo, A. F. Topological origin of subgap conductance in insulating bilayer graphene. *Nat. Phys.* **2011**, *7*, 38−42.
(28) Zhang, Y.; Brar, V. W.; Girit, C.; Zettl, A.; Crommie, M. F. Origin of spatial charge inhomogeneity in graphene. *Nat. Phys.* **2009**, *5*, 722−726.
(29) Monkhorst, H. J.; Pack, J. D. Special points for Brillouin-zone integrations. *Phys. Rev. B* **1976**, *13*, 5188−5192.
(30) Loring, T. A. K-Theory and Pseudospectra for Topological Insulators. *Ann. Phys.* **2015**, *356*, 383−416.
(31) Loring, T. A.; Schulz-Baldes, H. Finite volume calculation of K-theory invariants. *N.Y. J. Math.* **2017**, *23*, 1111−1140.
(32) Loring, T. A.; Schulz-Baldes, H. The spectral localizer for even index pairings. *J. Noncommutative Geometry* **2020**, *14*, 1−23.
(33) Cerjan, A.; Loring, T. A. Classifying photonic topology using the spectral localizer and numerical K-theory. *APL Photonics* **2024**, *9*, No. 111102.
(34) Cerjan, A.; Loring, T. A.; Schulz-Baldes, H. Local Markers for Crystalline Topology. *Phys. Rev. Lett.* **2024**, *132*, No. 73803.
(35) Weyl, H. Das asymptotische Verteilungsgesetz der Eigenwerte linearer partieller Differentialgleichungen (mit einer Anwendung auf die Theorie der Hohlraumstrahlung). *Math. Ann.* **1912**, *71*, 441−479.
(36) Bhatia, R. *Matrix Analysis (Graduate Texts in Mathematics)* Springer New York: New York, NY, 1997; Vol. *169*.
(37) Cerjan, A.; Loring, T. A.; Vides, F. Quadratic pseudospectrum for identifying localized states. *J. Math. Phys.* **2023**, *64*, No. 023501.
(38) Thouless, D. J. Anderson's theory of localized states. *J. Phys. C: Solid State Phys.* **1970**, *3*, No. 1559.
(39) Anderson, P. W. Absence of Diffusion in Certain Random Lattices. *Phys. Rev.* **1958**, *109*, 1492−1505.
(40) Moldovan, D.; Andelković, M.; Peeters, F. *pybinding v0.9.5: a Python Package For Tight-binding Calculations*, Zenodo 2020.
(41) Groth, C. W.; Wimmer, M.; Akhmerov, A. R.; Waintal, X. Kwant: a software package for quantum transport. *New J. Phys.* **2014**, *16*, No. 063065.
(42) Datta, S. *Electronic Transport in Mesoscopic Systems (Cambridge Studies in Semiconductor Physics and Microelectronic Engineering)*; Cambridge University Press, 1995.
(43) Anderson, P. W.; Thouless, D. J.; Abrahams, E.; Fisher, D. S. New method for a scaling theory of localization. *Phys. Rev. B* **1980**, *22*, 3519−3526.
(44) Beenakker, C. W. J. Random-matrix theory of quantum transport. *Rev. Mod. Phys.* **1997**, *69*, 731−808.
(45) Thouless, D. J. Localization distance and mean free path in one-dimensional disordered systems. *J. Phys. C: Solid State Phys.* **1973**, *6*, No. L49.

https://doi.org/10.1021/acsami.5c19865
ACS Appl. Mater. Interfaces 2026, 18, 6111−6121

(46) Chung, Y. J.; Villegas Rosales, K. A.; Baldwin, K. W.; Madathil, P. T.; West, K. W.; Shayegan, M.; Pfeiffer, L. N. Ultra-High-Quality Two-Dimensional Electron Systems. *Nat. Mater.* **2021**, *20*, 632−637.

https://doi.org/10.1021/acsami.5c19865
ACS Appl. Mater. Interfaces 2026, 18, 6111−6121